ORIGINAL PAPER

CrossMark

Immobilization of Fe_3O_4/TiO_2 nanocomposite thin layer on the glass tubes in a component parabolic collector for the treatment of DR23

L. Ghalamchi[1] · M. H. Rasoulifard[1]

Abstract

Photocatalysis driven by the natural solar light has been proved to be a favorable approach for the degradation of hazardous organic pollutants in water and wastewater. The present work addressed the removal of Direct Red 23 by the solar/Fe_3O_4/TiO_2/$S_2O_8^{2-}$ process. The application of the component parabolic collector, which served as a solar light concentrator, could improve the photocatalytic removal efficiency in the presence of immobilized Fe_3O_4/TiO_2 nanoparticles. In this paper, the synthesis of Fe_3O_4/TiO_2 photocatalyst to treat wastewater under solar radiation has been reported. Accordingly, a component parabolic collector solar photoreactor was designed and constructed for wastewater treatment processes. The prepared Fe_3O_4/TiO_2 nanocomposite was precipitated as a thin layer on the glass tubes of the solar photoreactor. The central composite experimental design was also used in order to optimize and model the CI Direct Red 23 decolorization process; then, the influence of operational parameters such as the contaminant concentration, $S_2O_8^{2-}$ concentration, and the reaction time was investigated. Due to the solar/Fe_3O_4/TiO_2/$S_2O_8^{2-}$ process, 100% of Direct Red 23 could be removed in 90 min at the concentration of 15.16 mg L^{-1} and $S_2O_8^{2-}$ concentration of 0.8 mM. The predicted response for the Direct Red 23 decolorization efficiency in the optimal condition was obtained to be 98.50%, which was in a good agreement with the experimental response (100%).

Keywords Degradation · Optimization · Photocatalysis · Photoreactor

Introduction

Advanced oxidation processes, particularly photocatalysis, have been employed to degrade the low concentrations of pollutants. The main objective of these processes is completing the degradation of toxic contaminants and converting them to safer products or products with lower toxicity (Ghaly et al. 2001; Cerrato et al. 2019). Moreover, these processes have been commonly applied for the pre-treatment of biological components to transfer some non-biodegradable pollutants to biodegradable products; they have also been employed as the posttreatment of some chemical and physical treatment processes for completing the treatment processes. Titanium dioxide is known as a good photocatalyst

Editorial responsibility: M. Abbaspour.

✉ M. H. Rasoulifard
   m_h_rasoulifard@znu.ac.ir

[1] Water and Wastewater Treatment Research Laboratory, Department of Chemistry, University of Zanjan, Zanjan, Iran

that can be employed to remove organic pollutants from water and wastewater; this property is owing to its biological and chemical inertness, non-toxicity, the strong oxidizing power, the low cost and long stability against photo- and chemical corrosions, as well as the its considerable degradation capacity for organic contaminants (Bilal et al. 2018; Nakata and Fujishima 2012; Shahadat et al. 2015). Titanium dioxide has been commonly used in numerous environmental and energy-related fields. In addition, the TiO_2 photocatalytic process as a sustainable treatment technique is applied to implement the zero waste scheme in water and wastewater industry; this technique is even employed to remove the pollutants and bacteria existing on the wall surface and in the air (Wolfrum et al. 2002; Hassan et al. 2016; Ghalamchi et al. 2017). Despite this, owing to its high band gap, it is important to have the high power of UV light irradiation with a wavelength which is lower than 387 nm (Faisal et al. 2007; Daneshvar et al. 2007). This limits the application of sunlight and increases the cost of the treatment process. The visible light constitutes the major fraction of solar radiation, while UV light covers less than 5% of solar radiation energy

(Prato-Garcia et al. 2009; Pirhashemi and Habibi-Yangjeh 2013). Therefore, synthesizing visible-light-active photocatalyst can be very helpful. Doping TiO_2 with transition metals (Lv et al. 2009a, b) and mixing TiO_2 with sensitizers (Yang et al. 2000) are the two most important approaches used to develop the main part of the solar spectrum.

Fe_3O_4/TiO_2 was employed as the visible-light-sensitive photocatalyst in this research. However, it should be noted that the recovery of finely powdered Fe_3O_4/TiO_2 from the treated water can be a process which is both incomplete and time-consuming (Lv et al. 2009b). Immobilization of the photocatalyst on supports such as sand, clay, and zeolite is a suitable method to tackle this problem. To the best of our knowledge, for the first time, Fe_3O_4/TiO_2 nanocomposite has been immobilized in this study as a thin layer on the outer surface of chemically and physically modified glass tubes and used in a CPC photoreactor for the removal of CI Direct Red 23 (DR23) as a model synthetic contaminant.

The investigation of the light intensity is considered as one of the important factors in the photocatalytic water treatment. CPC is used to improve the intensity of light, both solar and visible light. In general, the solar concentrator is a parabolic reflective surface which provides concentrated rays of light that are focused on a certain path wherein a glass tube has been located on the center. These collectors are designed with surfaces facing toward the equator, and the tilted angle is adjusted to be almost equal to the latitude. Calculation of the optimum tilted angle is a required step to maximize the amount of the collected beam radiation and, consequently, the amount of energy. For this reason, following the sun as it moves each day is the best procedure. The advantages of the solar CPC system include intrinsic simplicity, cost-effectiveness, easy application, and the low capital investment (Moncayo-Lasso et al. 2008; Sciacca et al. 2011; Zhan et al. 2014).

In this research, Fe_3O_4/TiO_2 nanocomposite was synthesized and immobilized on the outer surface of modified glass tubes as a thin layer. For the cost-effective purification of polluted wastewater and the use of the renewable solar energy, the Fe_3O_4/TiO_2 nanocomposite/glass tubes were used in a CPC. DR23 was treated as the model dye pollutant in this study, and the decolorization was optimized and modeled by the central composite design of experiments (CCD).

Materials and methods

Titanium dioxide nanoparticles P-25 with the surface area of $55 m^2 g^{-1}$ were supplied by Evonik Degussa (Germany), and ferric chloride hexahydrate ($FeCl_3·6H_2O$), ferrous chloride tetrahydrate ($FeCl_2·4H_2O$), and NaOH were obtained from Merck Co. in an analytical grade. Glass tubes (borosilicate) were purchased from Sina glass Co., Iran. Direct Red 23 with $\lambda_{max} = 507$ nm was obtained from Alvan Sabet Co. and applied without further purification; it was obtained from Hamedan, Iran. The dye solution was prepared using distilled water. The structure of organic dye is shown in Fig. 1.

Synthesis of the Fe_3O_4/TiO_2 nanocomposite

For the preparation of the Fe_3O_4/TiO_2 nanocomposite, $FeCl_3·6H_2O$ solution with the concentration of 1 M and $FeCl_2·4H_2O$ solution with the concentration of 2 M were mixed in a 100-mL beaker containing 0.5 g TiO_2 P25; the mixture was placed in a 150-W ultrasonic bath (the bath temperature was 60 °C) under nitrogen gas stream (Wu et al. 2011).

Then, 25 mL of the sodium hydroxide solution (1 M) was charged into the prepared suspension; as soon as the sodium hydroxide was added, black magnetite was obtained (Du et al. 2006). In order to complete the reaction, the mixture was sonicated for 30 min. Black sediments were collected through magnetic separation and washed by deionized water several times to reduce the pH to the neutral value and dried at 70 °C for 6 h in a vacuum oven.

## Immobilization of the TiO_2/Fe_3O_4 nanocomposite on the outer surface of glass tubes

At first, the outer surface of glass tubes with 1.5 cm diameter and 114 cm length was sanded by the SiC stone manually and placed in a 5% HF solution for 2 h; then, they were washed with distilled water. Finally, the tubes were placed for 15 min in the 1 M NaOH solution for enhancing the −OH groups at their surface.

Heat attachment (PMTP) approach was used for photocatalyst immobilization on the outer surface of the glass tubes. For the immobilization of nanoparticles on the glass tubes, 33.0 g/L of TiO_2/Fe_3O_4 nanocomposite was dispersed in ethanol (1.65 g nanocomposite in 50 mL ethanol) and sonicated for 20 min using the ultrasonic bath (150 W). The prepared suspension was poured on the outer surface of the glass tubes. The amount of the material deposited per unit area was approximately $0.0015 g cm^{-2}$, with the assumption of no wastage of nanoparticles. The following drying at room temperature, the tubes were heated at the temperature of 480 °C for 3 h. The tubes were washed with distilled water and that process was repeated for the better immobilization of the nanocomposite. The structural characteristics of TiO_2/Fe_3O_4 nanophotocatalysts were investigated using X-ray, diffraction (Siemens D-500 system (Germany), Cu Ka radiation at the wavelength of 0.15406 nm, 40 kV, and 30 mA). The average crystallite size of Fe_3O_4 particles was estimated by the Scherer's formula (Rasouli et al. 2014)

$$d = \frac{k \times \lambda}{\beta \times \cos\theta},$$ (1)

Fig. 1 Structure of DR23 a) hydrazone tautomeric form and b) azo form

hydrazo-hydrazo

azo-azo
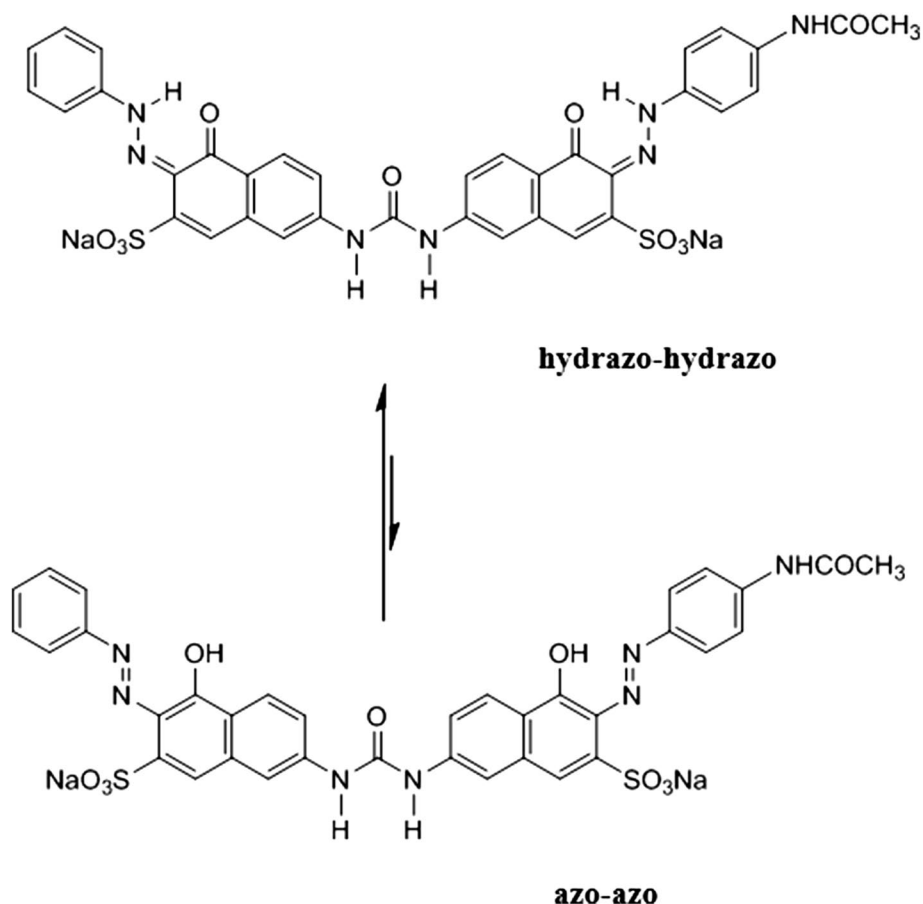
where d is the average crystalline size, k is a constant (0.9), λ is the wavelength of the X-ray radiation, β is the line width at the half maximum in terms of 2θ, and θ is the Bragg diffraction angle in degree.

The morphology of the glass tubes after physical and chemical modification and after TiO_2/Fe_3O_4 coating was examined by a field emission scanning electron microscope using a MIRA3 FEG-SEM Tescan (Czech). Energy-dispersive X-ray spectroscopy (EDS) was also used to confirm the synthesis of the TiO_2/Fe_3O_4 nanocomposite using a MIRA3 Tescan (Czech).

The band gaps of TiO_2, Fe_3O_4, and Fe_3O_4/TiO_2 nanocomposites were determined using the UV–Vis spectrophotometer (Shimadzu UV-160). Accordingly, each sample was dispersed in distilled water through sonication for 15 min in order to form a homogeneous suspension. Subsequently, recording of the optical absorption spectra of the samples was done in wavelengths ranging from 200 to 700 nm and at the room temperature. The band gap of TiO_2, Fe_3O_4, and Fe_3O_4/TiO_2 nanocomposites was determined through Eq. (2):

$$(Ah\upsilon)^2 = K\left(h\upsilon - E_g\right) \tag{2}$$

In this equation, $h\upsilon$ is the photon energy (eV), A refers to the absorption coefficient, K is a constant, and E_g denotes the band gap. The band gap could be calculated by the extrapolation of the linear region in a plot of $(Ah\upsilon)^2$ versus photon energy.

Design of the solar photoreactor

In this present study, a CPC reactor was constructed and used for the dye solution treatment. The reactor consisted of two parts, a reflective made of stainless steel and a receiver consisting of a borosilicate glass tube. Two concentric borosilicate glass tubs were placed in the focal path of the CPC with the maximum radiation. The total length of the reactor was 114 cm. The inner tube had the diameter of 1.5 cm, while that of the outer one was 3.5 cm. The prepared nanocomposite was immobilized on the outer surface of the inner tube. The contaminated water was moving between the two tubes. The total volume of the contaminated water was 1500 mL, while 950 mL of water was exposed to the sunlight irradiation at a time. This CPC was placed on the ramp at 39° (around the local latitude) from the horizon, so there was no need for the solar tracking (Fig. 2).
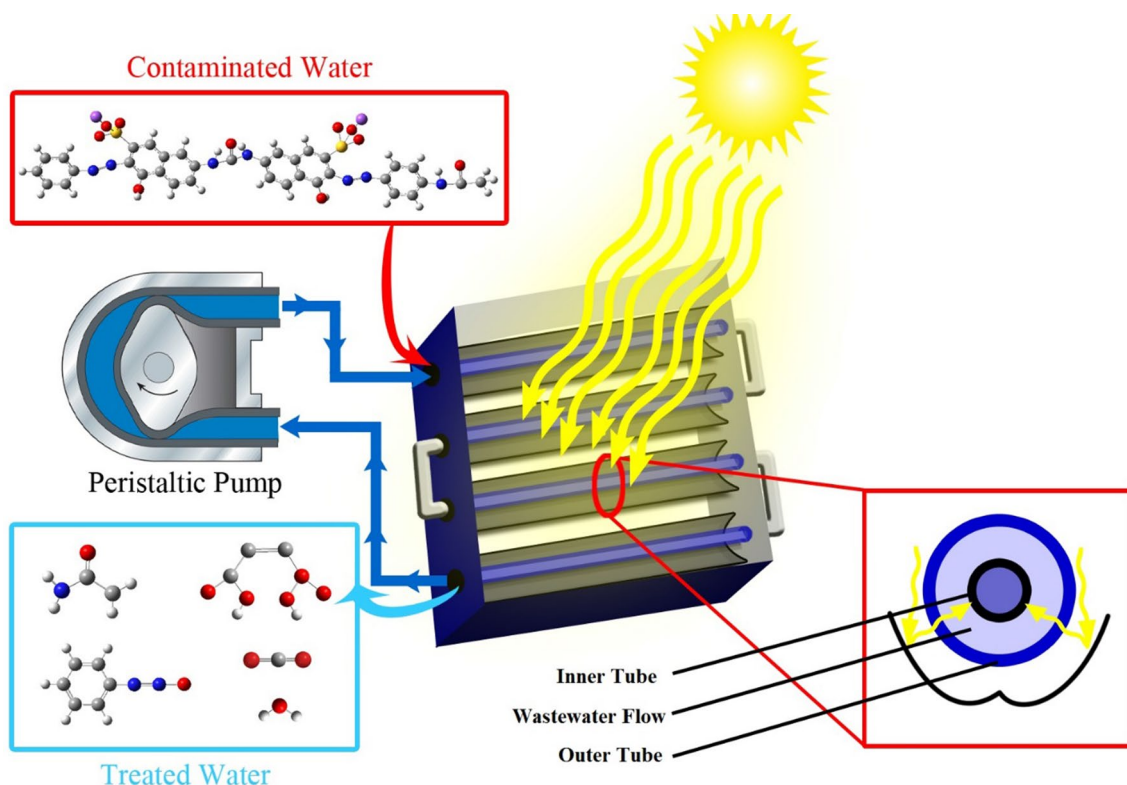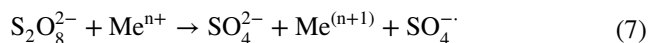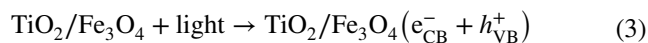
Fig. 2 Schematic different parts of component parabolic collector: reflector and absorber pipe

Treatment procedure

In the present work, after the preparation of the dye solution and addition of the determined amount of the oxidizing agent, $S_2O_8^{2-}$, the solution was poured into the reservoir. The injection of the contaminated solution into the parabolic reactor was done by employing a peristaltic pump having the constant flow rate of 40 mL min^{-1}. The same immobilized nanoparticles on the glass tubs in the CPC were used in all experiments, and no new photoreactor was replaced each time. In the first series of the experiments with the same condition of an experiment, the performance of the photoreactor was not dropped over time, and it was negligible at least during the 30 times and the experiments were carried out. The reactions were performed between 11 A.M. and 3 P.M. to provide the maximum light intensity. The UV index was constant during the experimental days. The reactor was placed on the roof of University of Zanjan. The reaction time was considered from the moment at which the dye solution was exposed to the sun irradiation. The decolorization efficiency was calculated by measuring the dye concentration at the beginning and end of the reaction using spectrophotometric analysis. The dye solution was circulated in the parabolic reactor in the course of conducting the experiment. For all 20 experiments, this process was repeated, which had been designed by RSM. In addition, chemical oxygen demand (COD) analysis was also carried out by using the spectrophotometer (DR/2000 direct reading spectrophotometer), based on the Standard Methods (1985) section 5220 D. Equations (3)–(8) show the probable chemical reactions for dye degradation (Epold and Dulova 2015; Bekkouche et al. 2017). The dye solution was circulated in the parabolic reactor during the experiment. This process was repeated for all 20 experiments designed by RSM. Chemical oxygen demand (COD) analysis was also measured using the spectrophotometer (DR/2000 direct reading spectrophotometer), according to the Standard Methods (1985) section 5220 D. The probable chemical reactions for dye degradation have been listed as shown in Eqs. (3)–(8) (Epold and Dulova 2015; Bekkouche et al. 2017)

$$TiO_2/Fe_3O_4 + light \rightarrow TiO_2/Fe_3O_4\left(e_{CB}^- + h_{VB}^+\right) \tag{3}$$

$$S_2O_8^{2-} + h\nu \rightarrow 2SO_4^{-\cdot} \tag{4}$$

$$SO_4^- + e^- \rightarrow SO_4^- \tag{5}$$

$$SO_4^{-\cdot} + H_2O \rightarrow HSO_4^- + OH^\cdot \tag{6}$$

$$S_2O_8^{2-} + Me^{n+} \rightarrow SO_4^{2-} + Me^{(n+1)} + SO_4^{-\cdot} \tag{7}$$

$$2Fe^{2+} + S_2O_8^{2-} \rightarrow 2Fe^{3+} + 2SO_4^{-\cdot} \tag{8}$$

Measurement of CI Direct Red 23

The absorbance of the DR23 aqueous solution was recorded in the wavelength range of 200–800 nm and 507 nm; it was obtained as the maximum absorbance–wavelength. Calibration curve of DR23 was prepared using known aqueous solutions with different concentrations (10, 15, 20, 30, 40, 50 mg L^{-1}) and their absorbance values at 507 nm. This curve was employed in order to convert the absorbance data to the dye concentration based on the Beer–Lambert law. By applying Eq. (9), the removal efficiency of the dye was obtained:

$$R(\%) = \frac{C_0 - C_t}{C_0} \times 100, \tag{9}$$

where R is the dye decolorization efficiency of DR23 and C_0 and C_t (mg L^{-1}) is the concentration of DR23 solution before and after treatment, respectively.

The central composite design of the photocatalytic process

The central composite design (CCD) with three variables in five levels was employed in this study. For three variables, 20 experiments were considered in the CCD design. Tables 1 and 2 illustrate the complete design matrix of this experimental design. In the present research, the CCD design was performed using Minitab 16.1. The factors which were considered in this experiment included DR23 initial concentration (x_1), S$_2$O$_8^{2-}$ concentration (x_2), and reaction time (x_3). We can approximate the mathematical relationship existing between the decolorization efficiency (as response, y) and the three significant independent variables, namely x_1, x_2, and x_3, by using a nonlinear polynomial model including 3 linear, 3 square, and 3 two-factor interaction terms and 1 intercept term, as can be seen in Eq. 10 (Blanco et al. 1999; Khataee et al. 2010; Aber and Sheydaei 2012; Amani-Ghadim et al. 2013):

$$y = \beta_0 + \sum_{i=1}^{k} \beta_i x_i + \sum_{i=1}^{k} \beta_{ii} x_i^2 + \sum_{i=1}^{k-1} \sum_{j=2}^{k} \beta_{ij} x_i x_j + \varepsilon, \tag{10}$$

Table 1 Original and uncoded levels of the input variables

Parameter	Levels				
	−2	−1	0	+1	+2
(X_1) Dye	15	22.5	30	37.5	45
(X_2) S$_2$O$_8^{2-}$	0.2	0.6	1	1.4	1.8
(X_3) Time	10	30	50	70	90

Table 2 CCD, experimental plan, and results

Std order	Run order	Dye (mg L^{-1})	S$_2$O$_8^{2-}$ (mM)	Time (min)	Decolorization percentage (%)	
					(Exp[a])	(Pre[b])
20	1	30.0	1.0	50	54.0	51.9
10	2	45.0	1.0	50	32.3	33.5
19	3	30.0	1.0	50	53.0	51.9
3	4	22.5	1.4	30	58.0	60.3
13	5	30.0	1.0	10	23.8	23.7
2	6	37.5	0.6	30	17.9	17.3
14	7	30.0	1.0	90	77.0	75.1
6	8	37.5	0.6	70	34.0	33.7
17	9	30.0	1.0	50	53.2	51.9
11	10	30.0	0.2	50	12.8	12.3
5	11	22.5	0.6	70	55.3	57.9
1	12	22.5	0.6	30	32.0	33.1
12	13	30.0	1.8	50	71.4	69.7
18	14	30.0	1.0	50	51.5	51.9
8	15	37.5	1.4	70	63.0	63.9
15	16	30.0	1.0	50	50.0	51.9
16	17	30.0	1.0	50	52.0	51.9
4	18	37.5	1.4	30	37.9	37.3
9	19	15.0	1.0	50	84.0	80.7
7	20	22.5	1.4	70	92.8	95.3

[a]Experimental
[b]Predicted

where y is the DR23 decolorization efficiency, β_0 is the constant coefficient, β_1, β_2, and β_3 are the linear effects of the variables x_1, x_2, and x_3, respectively, β_{11}, β_{22}, and β_{33} represent quadratic effects, and β_{12}, β_{13}, and β_{23} refer to the interaction effects of the variables.

Results and discussion

Characterizations of TiO₂/Fe₃O₄ on the glass tubes

The XRD pattern of the synthesized TiO_2/Fe_3O_4 glass tube is shown in Fig. 3. The Fe_3O_4 peaks were observed at $2\theta = 30.1, 35.4, 37.0, 43.0, 53.3,$ and 56.9 corresponding to the crystal planes of (220), (311), (222), (400), (422), and (511), respectively. As shown by the strong and sharp peaks, the formation of iron oxide with a cubic inverse spinel structure that was consistent with the standard data for magnetite could be confirmed (JCPDS card no. 00-019-0629).

From Eq. 1, the average crystalline size of the prepared Fe_3O_4 was estimated. This equation was applied to the maximum intensity peak (311) of the pattern, and the crystalline size was calculated to be approximately 21 nm.

XRD of the TiO_2/Fe_3O_4 nanocomposite on the glass tube is illustrated in Fig. 3, indicating TiO_2 standard peaks ($2\theta = 25.0, 37.5, 47.2,$ and 54.1) in addition to Fe_3O_4 peaks. Both rutile and anatase phases of TiO_2 were present in this study. Regarding XRD analysis, the (101) and (200) peaks which were located at 2θ of $25.4°$ and $48.24°$ were related to the anatase phase of TiO_2 (JCPDS No. 21-1272). The rutile phase could also be identified from its (110) peak, which was located at 2θ of $27.4°$ in the XRD pattern. These results confirmed the synthesis of Fe_3O_4 and TiO_2/Fe_3O_4 nanoparticles on the glass tube.

The FTIR spectrum of the synthesized Fe_3O_4, TiO_2, and TiO_2/Fe_3O_4 nanocomposites in a range from 500 to 4000 cm^{-1} is depicted in Fig. 4. A broad peak around 577 cm^{-1} could be attributed to the stretching vibration of Fe–O, which was well matched with the main peak of magnetite. Peaks near 3418 cm^{-1} were related to the hydroxyl groups on the surface of TiO_2. The characteristic band of TiO_2, in the region 500–700 cm^{-1}, was also detected, which could be assigned to the Ti–O–Ti stretching vibrations of the TiO_2/Fe_3O_4 nanocomposite. The presence of water could be proved by the absorption peak at 1633 cm^{-1}, which corresponded to the bending H–O–H. Both the pure TiO_2 and Fe_3O_4 peaks could be seen, confirming the synthesis of the TiO_2/Fe_3O_4 nanocomposite.

According to Fig. 5, EDS spectra of immobilized TiO_2/Fe_3O_4 confirmed the presence of Ti, Fe, and O elements on

Fig. 3 XRD analysis of Fe_3O_4 and TiO_2/Fe_3O_4 synthesized nanoparticles

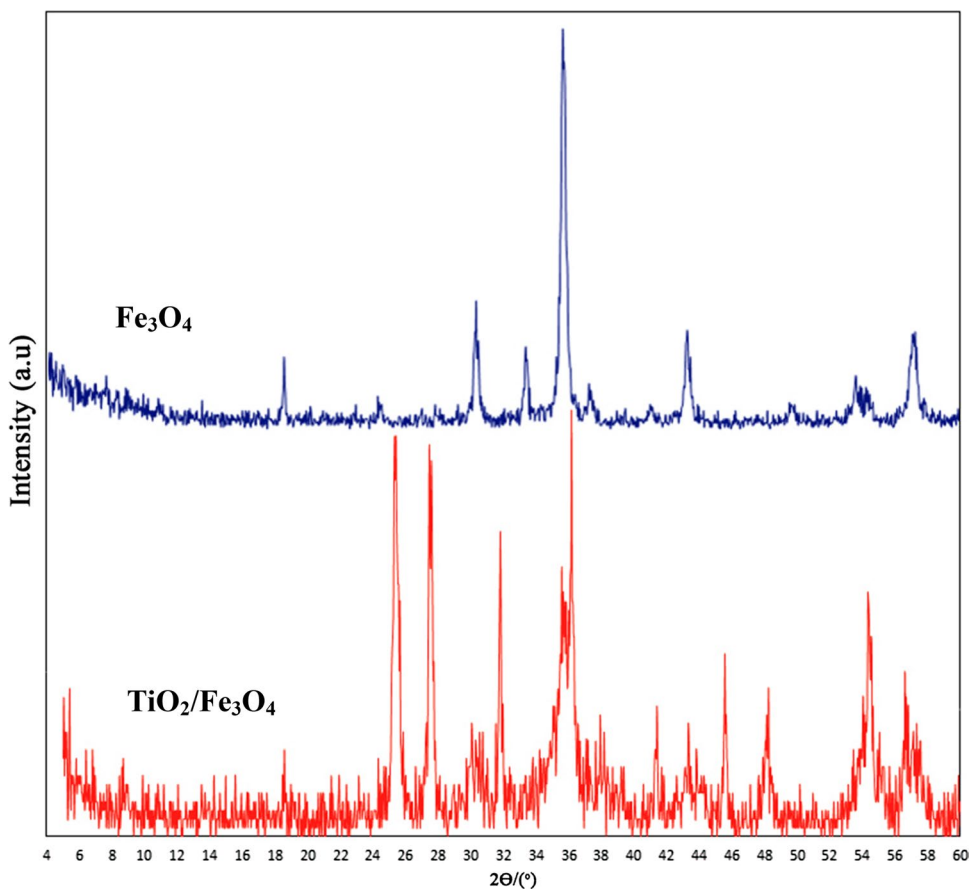**Fig. 4** FTIR analysis of TiO_2, Fe_3O_4, and TiO_2/Fe_3O_4 synthesized nanoparticles

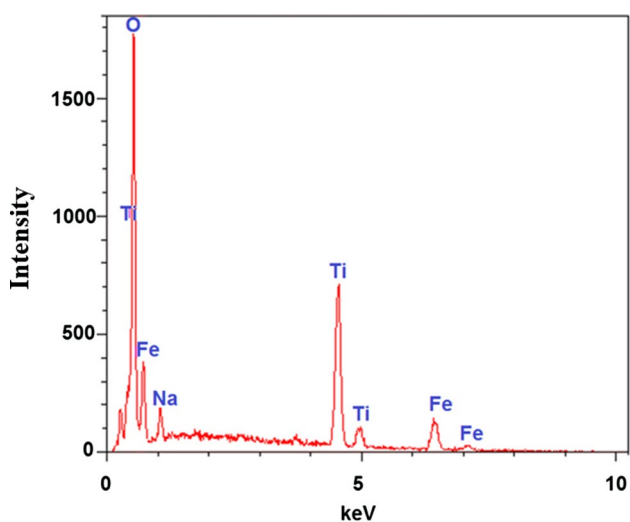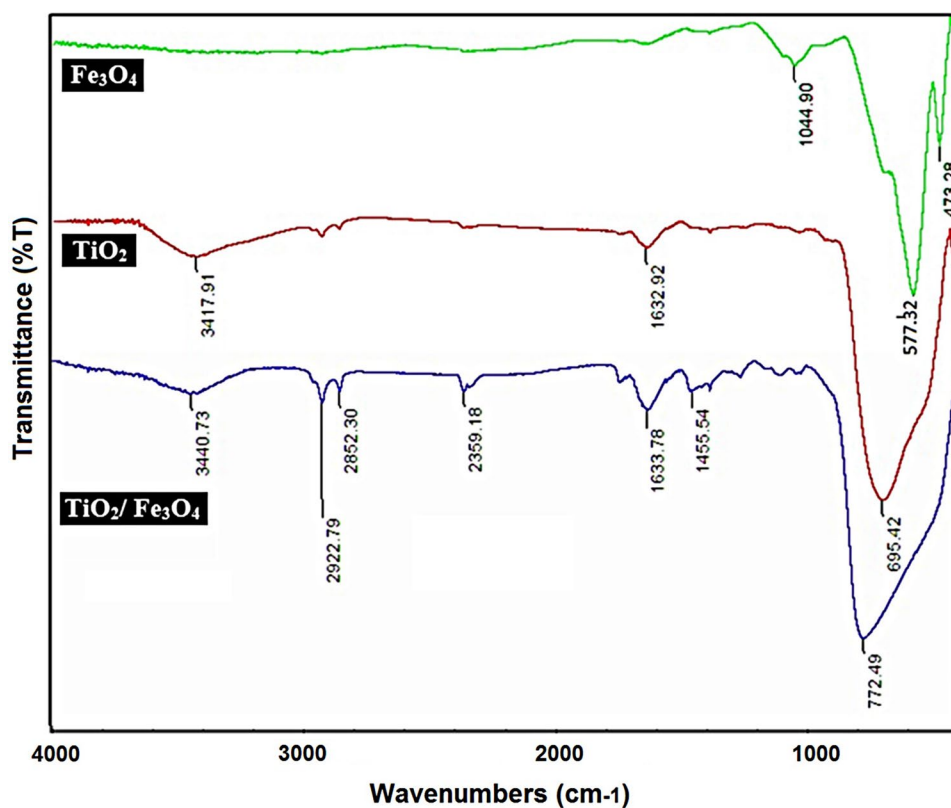**Fig. 5** EDS analysis of immobilized TiO_2/Fe_3O_4

the glass tubes. SEM images of the outer surface of glass tubes after physical and chemical modification are illustrated in Fig. 6a, b with two magnifications. These figures indicate the porosity at the surface of glass, which could be attributed to the physical and chemical modification with SiC stone and HF.

SEM images of the outer surface of the glass tubes after TiO_2/Fe_3O_4 thin-layer immobilization are demonstrated in

Fig. 6c, d. Comparison of these images with the previous two ones confirmed the immobilization of the nanocomposite on the surface of the glass tubes. In this research, there was no characterization that could determine the thickness of the thin layer of nanocomposite on the glass tubes. Moreover, the thin layer of the immobilized nanoparticles was non-uniform.

Figure 7 represents the DRS spectra of the pure TiO_2 and Fe_3O_4/TiO_2 nanocomposite. The band gap of the pure TiO_2 was estimated to be 3.2 eV, which corresponded to wavelengths shorter than 390 nm. This was in agreement with the previous reports (Khaki et al. 2018). As shown in Fig. 7, the energy band gap of the Fe_3O_4/TiO_2 nanocomposite was 2.6 eV; this was lower than that of the pure TiO_2. Therefore, the Fe_3O_4/TiO_2 nanocomposite was suitable as a photocatalyst under sunlight irradiation for the water treatment.

The removal efficiency of the photocatalyst

To study the importance of the photocatalyst, the decolorization of DR23 was performed using the $S_2O_8^{2-}$, $TiO_2/S_2O_8^{2-}$, TiO_2/Fe_3O_4 nanocomposite, and the TiO_2/Fe_3O_4 nanocomposite in the presence of $S_2O_8^{2-}$. The effect of light was also studied in this test. For this purpose, each of the above experiments was done in a dark condition for 30 min; then, this was continued under solar light. The results of these experiments are illustrated in Fig. 8.

Fig. 6 FE-SEM images of outer surface of glass tube after preparation for nanoparticles immobilization (**a**, **b**), FE-SEM images of TiO$_2$/Fe$_3$O$_4$ immobilization (**c**, **d**)
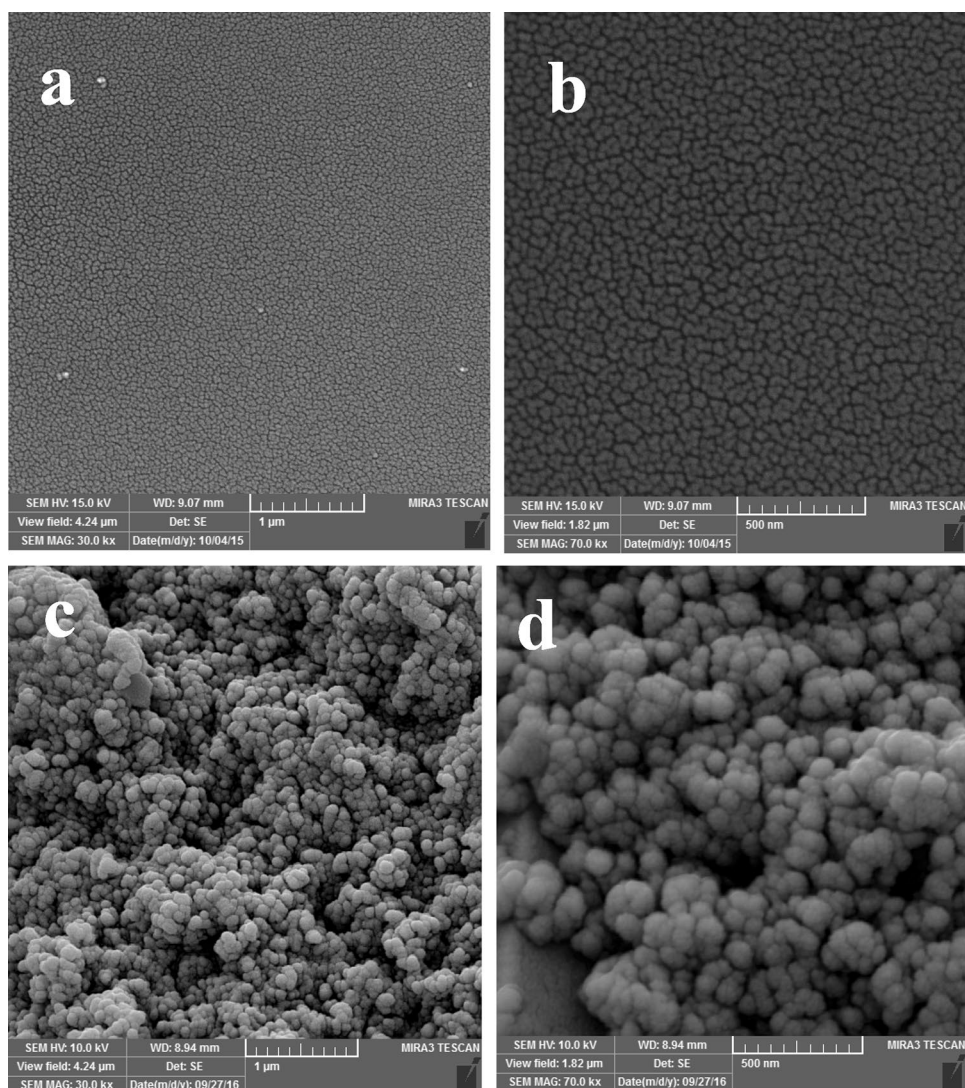
According to this figure, in the dark condition, no significant decolorization was observed in all of the above conditions, indicating the importance and necessity of light for the photocatalytic process. Under the solar radiation, the TiO$_2$/Fe$_3$O$_4$ nanocomposite in the presence of S$_2$O$_8^{2-}$ showed the best performance. It was found that both light and the semiconductor photocatalyst were required to effectively remove the dye from water solution (Zamiri et al. 2014; Eskandarian et al. 2016). It was shown that solar irradiation led to exciting the electron from the valence band of the TiO$_2$/Fe$_3$O$_4$ nanocomposite to the conduction band; then, the formation of an electron–hole pair occurred on the surface of the catalyst (Eq. 3) (Behnajady et al. 2006), leading to active radicals production.

The decolorization of DR23 was evaluated with and without the addition of S$_2$O$_8^{2-}$ as the assistant agent in order to investigate the catalytic performance of Fe$_3$O$_4$/TiO$_2$.

Sulfate radicals were produced by irradiating light beams on the peroxydisulfate ions (Eq. 4); further, it could be attributed to the interaction of sulfate radicals with the conductive bond electrons (e_{cb}^-); this was, in turn, due to the collision of the light beams with the Fe$_3$O$_4$/TiO$_2$ nanocomposite surface (Eq. 5). The $^.OH$ radicals were yielded as a result of the reaction of the sulfate radicals with the H$_2$O molecules (Eq. 6). More reaction could take place. The mentioned production of the radicals led to the more removal of the dye molecules.

In addition to the mentioned reactions, sulfate radicals were generated from the reaction between transition metals like Fe^{2+} in Fe$_3$O$_4$ and S$_2$O$_8^{2-}$, as mentioned in Eqs. 7 and 8.

Due to more sulfate radicals production in the solar/TiO$_2$/Fe$_3$O$_4$/S$_2$O$_8^{2-}$ process, as compared with the solar/S$_2$O$_8^{2-}$ treatment process, the dye removal was improved in the presence of the nanocomposite.
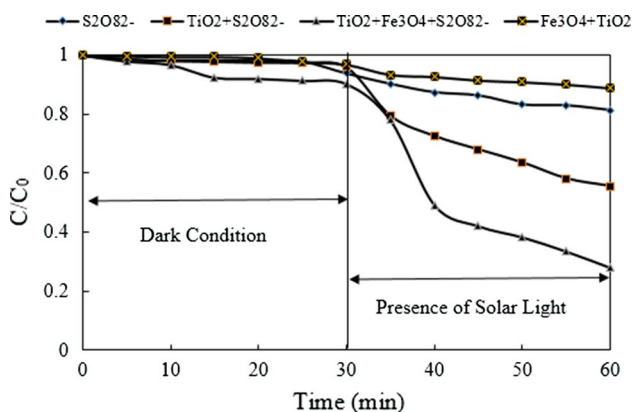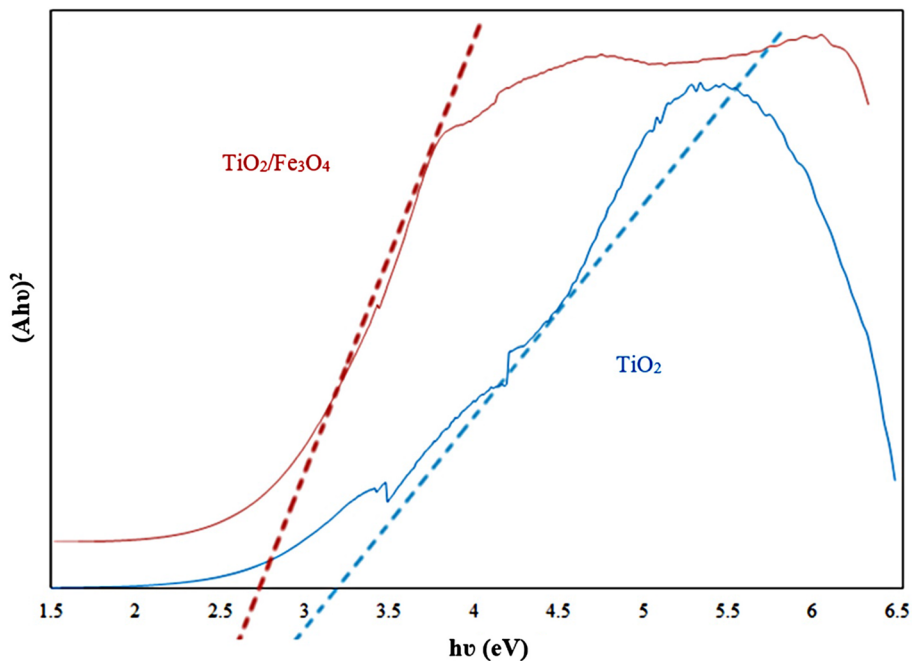
Fig. 7 Estimated band gap of pure TiO_2 and TiO_2/Fe_3O_4

Fig. 8 Effect of presence of only $S_2O_8^{2-}$ and each of nanoparticles with $S_2O_8^{2-}$ on removal of DR23

Analysis of variance

The experiments were conducted based on the central composite experimental design. The application of the response surface methodology for this design and the experimental results yielded the following polynomial equation:

$$y = 7.71 - 1.65x_1 + 72.04x_2 + 0.90x_3$$
$$+ 0.02x_1^2 - 17.02x_2^2 - 0.01x_3^2 - 0.60x_1x_2, \quad (11)$$

where y is the DR23 decolorization efficiency and x_1, x_2, and x_3 are the variables referring to the amount of DR23 initial concentration, $S_2O_8^{2-}$ concentration, and the reaction time, respectively.

We employed the analysis of variance (ANOVA) in order to evaluate the adequacy of the polynomial model. Table 3 lists ANOVA results of this quadratic model. To check the significance of each coefficient, the probability value (p value) was used. A p value less than 0.05 at 95% confidence level indicated that the model terms were significant. The p value analysis of the regression showed that all of the linear model terms (x_1, x_2, and x_3), the quadratic terms of x_1^2 and x_2^2, and the interaction terms of $x_1 \times x_3$ and $x_2 \times x_3$ were important (with a p value less than 0.05), while x_3^2 and $x_1 \times x_2$ terms were meaningless (with a p value larger than 0.05) in the DR23 decolorization process in the CPC (Table 4).

Table 3 ANOVA for fit of decolorization efficiency from CCD

Source of variation	Sum of squares	DOF	Adj SS	Adj MS	F value	P value
Regression	8564.12	9	8564.12	951.569	185.88	0.000
Residual total	51.19	10	51.19	5.119		
Total	8615.31	19				
Lack of fit	40.99	5	40.99	8.197	4.01	0.077

$R^2 = 99.41\%$ R^2 (adj) $= 98.87\%$

Table 4 Factor effects and associated *P* values and *T* values

| Term		Coefficient	P value	T value
Constant	β_0	7.7149	0.000	0.5
Dye	β_1	− 1.6521	0.023	− 2.682
$S_2O_8^{2-}$	β_2	72.0386	0.000	6.501
Time	β_3	0.9026	0.002	4.073
Dye × dye	β_{11}	0.0231	0.000	2.875
$S_2O_8^{2-} \times S_2O_8^{2-}$	β_{22}	− 17.0256	0.017	− 6.037
Time × time	β_{33}	− 0.0016	0.000	− 1.416
Dye × $S_2O_8^{2-}$	β_{12}	− 0.6038	0.187	− 2.264
Dye × time	β_{13}	− 0.014	0.007	− 2.627
$S_2O_8^{2-}$ × time	β_{23}	0.3202	0.047	3.202
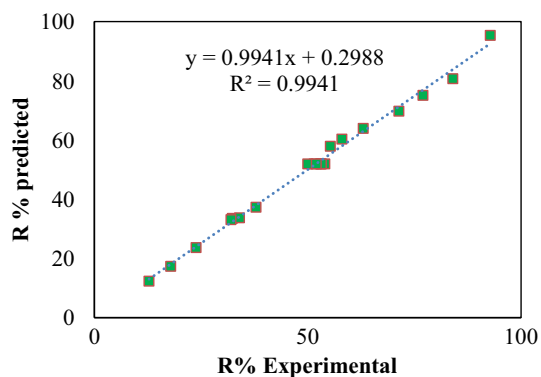
Fig. 9 Comparison of the experimental results of decolorization efficiency with those calculated via CCD results equation

According to Table 4, the Fischer's value (*F*-test) of the quadratic model was 185.88; this was found to be higher than the related critical value for degrees of freedom equal to 9 and 10, at the significance level of 0.05 ($F_{\text{crtical},0.05,9,10} = 2.04$). Therefore, the model could predict the effect of changing the input parameters on the photocatalytic decolorization of DR23 using the Fe_3O_4/TiO_2 nanocomposite in a CPC.

Furthermore, the high *p* value (0.077) and the low *F* value (4.01) for the lack-of-fit term revealed the insignificant lack of fit of the model, thereby confirming its sufficient accuracy in predicting the response.

The suitability of the constructed model was also verified by the determination coefficient ($R^2 = 0.99$) (Fig. 9). The R^2 close to unity showed a good agreement between the experimental and predicted data, implying that the model was adequate, such that more than 99% of the total variations could be explained by the model (Yousef et al. 2012).

The reliability of the model was examined by the residual plots (Fig. 10). The pattern of the straight line in the normal plot of the residuals implied a normal distribution of the errors (Sheydaei et al. 2014). The same scattering pattern above and below the axis could be seen from the residuals against the predicted values of the response. The histogram of the residuals for the DR23 decolorization process in CPC almost had a normal distribution, and the residuals versus the run order of the experiments could be useful to represent the random scattering of the residuals
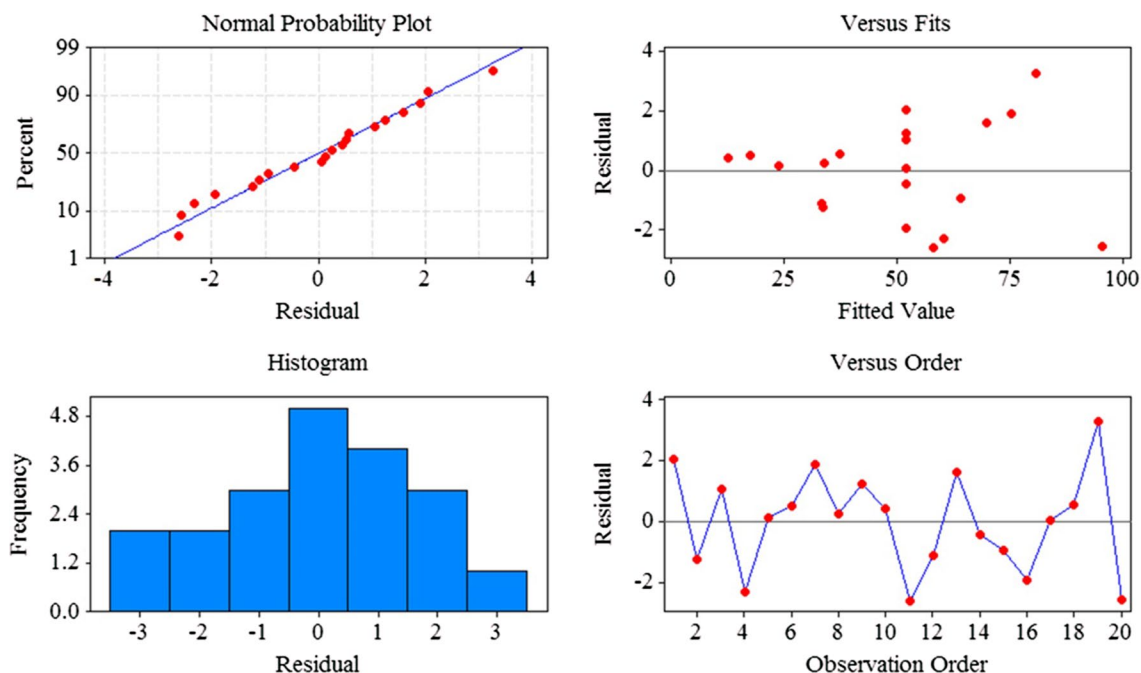
Fig. 10 Residual plots of examined model for DR23 decolorization

around zero; this implied that the obtained model was adequate for the DR23 decolorization process.

The effect of variables on DR23 decolorization

Three-dimensional (3-D) and contour plots are illustrated in Fig. 11 for the graphical interpretation of the effect of the variables on the response. 3-D surfaces and contour plots were plotted by considering two parameters variable at a time while keeping the other one at the central (0) level.

The effect of peroxydisulfate concentration

The $S_2O_8^{2-}$ concentration varied from 0.2 to 1.8 mM. As can be seen from Fig. 11a, b, e, and f, the decolorization efficiency of DR23 was enhanced with enhancing the initial
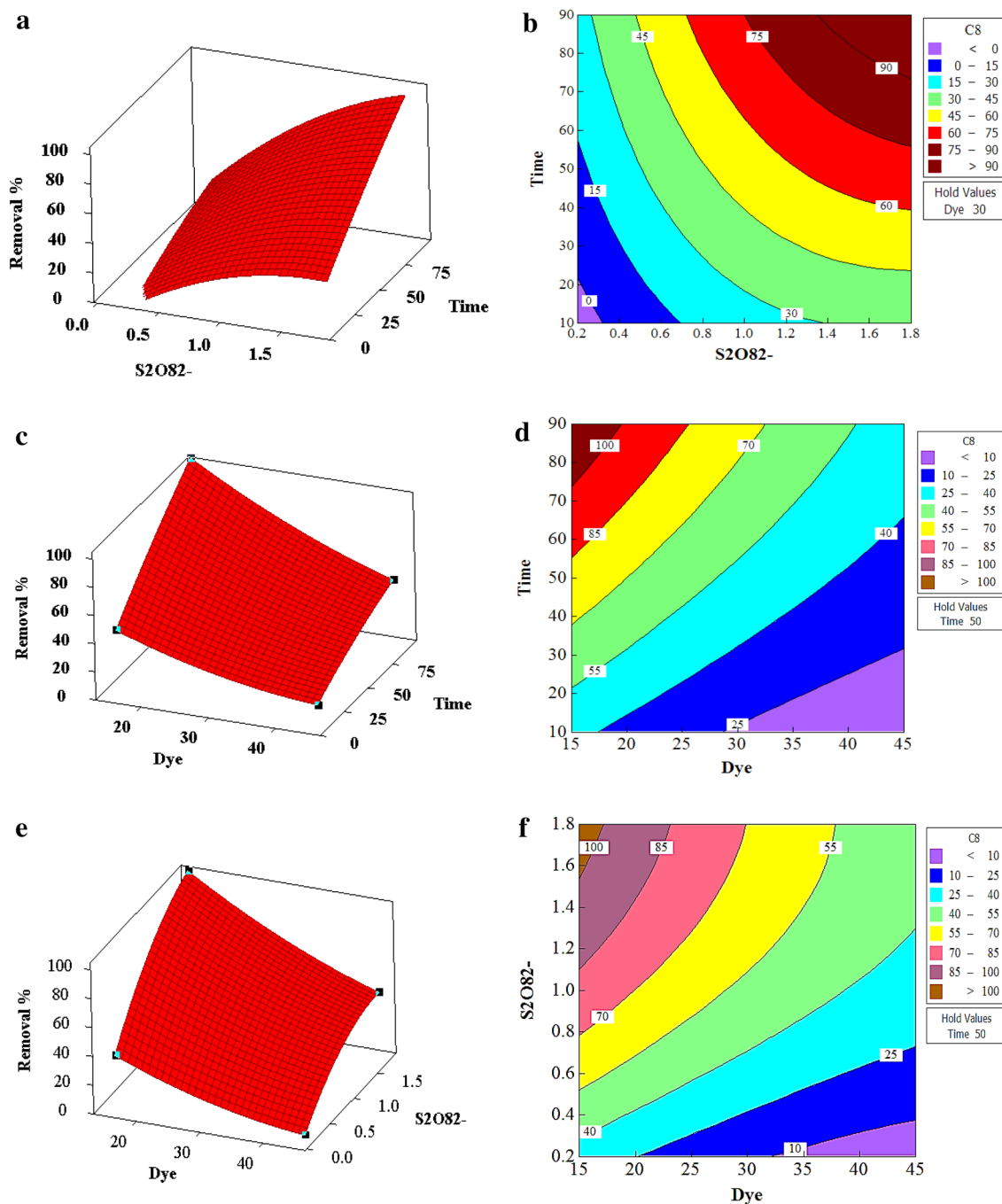

Fig. 11 Response surface plot and contour plot of the decolorization efficiency (R%) as the function of parameter

concentration of $S_2O_8^{2-}$ up to 1.0 mM. This was because of the generation of the more hydroxyl and sulfate oxidizing radicals. It is noteworthy that sulfate radicals were produced in both solar/$S_2O_8^{2-}$ (Eqs. 6–8) and solar/TiO$_2$/Fe$_3$O$_4$/ $S_2O_8^{2-}$ processes (Eqs. 9–10). At the higher concentrations of $S_2O_8^{2-}$, the decolorization efficiency was decreased due to the production of more hydroxyl and sulfate radicals, leading to the radical recombination, scavenging reaction, and subsequently the lower decolorization efficiency. Therefore, $S_2O_8^{2-}$ had the optimal concentration for the DR23 solution treatment in CPC.

The effect of the dye concentration

Initial DR23 concentration dependency was investigated by varying its concentration in the range of 15–45 mg L^{-1}. Based on the related 3-D and counter plots, it was found that the decolorization efficiency was lowered with enhancing the initial concentration of the dye. With increasing DR23 concentration, the light penetrating the photocatalyst surface was decreased; therefore, the generation of ˙OH was decreased too. Further, DR23 molecules absorbed or scattered some of the sun light, preventing them from reaching on the nanoparticles surface, which might be another possible reason to reduce the removal efficiency (Muruganandham et al. 2006; Sciacca et al. 2011).

The effect of the reaction time

The reaction time was changed from 10 to 90 min in order to address its effect on the pollutant removal efficiency. The decolorization efficiency was enhanced by increasing the reaction time. In fact, with increasing the reaction time, it was found that the residence time of the dye molecules in the photoreactor was enhanced, thereby allowing more reaction between ˙OH and sulfate radicals and the molecules of dye. So, the pollutant removal efficiency was enhanced (Bandala et al. 2008).

Optimized conditions for DR23 decolorization in a CPC using the Fe$_3$O$_4$/TiO$_2$ nanocomposite

Determination of the optimum values of the variables was the main purpose of the optimization by CCD. The optimum values of the parameters obtained by CCD were the DR23 initial concentration of 15.16 mg L^{-1}, the initial $S_2O_8^{2-}$ concentration of 0.8 mM, and the reaction time of 90 min. The predicted DR23 decolorization efficiency was 98.50% in the optimal condition. The experimental response in the predicted optimal condition was performed three times, and the average of them was 100.0%, near the value predicted by the model (Table 5).

Table 5 Comparison of experimental and predicted values of removal of DR23 at the optimal levels predicted by RSM

Optimal conditions		Predicted value (%)	Observed value (%)
(X_1) Dye	15.16 mg L^{-1}	100	98.5
(X_2) $S_2O_8^{2-}$	0.8 mM		
(X_3) time	90		

In the mineralization process, organic materials are eventually converted to CO_2 and H_2O (Modirshahla et al. 2007). Mineralization is often investigated by considering the total organic carbon (TOC), chemical oxygen demand (COD), and absorption at 254 nm measurements (Modirshahla et al. 2007; Marandi et al. 2012). COD criterion was used in the present study in order to evaluate the degree of mineralization (Modirshahla et al. 2007; Marandi et al. 2012). As the COD value is related to the total concentration of the organic materials in the solution, the reduction in it could show the extent of mineralization. Measuring the COD of the dye solution after the treatment process is very important in order to confirm whether the dye is mineralized. According to the literature (Saien et al. 2017; Dükkancı 2018), it is obvious that the photocatalytic process is more useful for decolorization, as compared with the degradation process and COD removal. In this work, 84% of COD was reduced during the Fe$_3$O$_4$/TiO$_2$/$S_2O_8^{2-}$ treatment process of DR23, showing the efficiency of the treatment procedure.

Reusability of the immobilized catalyst

Stability of nanoparticles in the successive applications is critical for practical usage. To confirm the catalyst reusability, the solar/TiO$_2$/Fe$_3$O$_4$/$S_2O_8^{2-}$ process for the decolorization of DR23 was repeated up to five other cycles. The decolorization efficiency was still high after several usages, as shown in Fig. 12. Before all experiments, the immobilized TiO$_2$/Fe$_3$O$_4$ nanocomposite released dosage was measured by the ICP method. The results revealed that only the released Ti concentration was lower than 2.3 mg L^{-1} after 90 min in the first five tests. In the first five tests, there could be a negligible release of nanoparticles, and a decline in the dye removal efficiency was observed. After that, a constant condition was observed. This was proved by repeating the experiments under the same conditions of the experiment.

Conclusion

This study showed that the heterogeneous photocatalysis (solar/Fe$_3$O$_4$/TiO$_2$) of DR23 had the best performance at 98.5% decolorization. According to the results, the
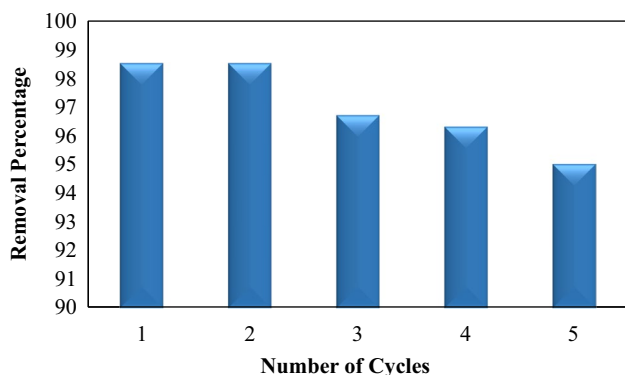
Fig. 12 Reusability of immobilized TiO_2/Fe_3O_4 $[S_2O_8^{2-}] = 0.8$ mM, $[DR23] = 15$ mg L^{-1}, Time $= 90$ min

immobilization of the nanocomposite on the outer surface of glass tubes and their applications in the component parabolic collector could have the potential to improve the conventional wastewater treatment. Moreover, the satisfactory goodness of fit between the predicted and experimental results reflected the applicability of the quadratic model in optimizing the treatment used in the decolorization process. Notably, better performance was obtained under the higher $S_2O_8^{2-}$ concentration. Due to the advantages of this process, it can be regarded as a candidate for fast and inexpensive water treatment technology.

Compliance with ethical standards

References

Aber S, Sheydaei M (2012) Removal of COD from industrial effluent containing indigo dye using adsorption method by activated carbon cloth: optimization, kinetic, and isotherm studies. Clean Soil Air Water 40:87–94. https://doi.org/10.1002/clen.201000434

Amani-Ghadim AR, Aber S, Olad A, Ashassi-Sorkhabi H (2013) Optimization of electrocoagulation process for removal of an azo dye using response surface methodology and investigation on the occurrence of destructive side reactions. Chem Eng Process Process Intensif 64:68–78. https://doi.org/10.1016/j.cep.2012.10.012

Bandala ER, Peláez MA, Salgado MJ, Torres L (2008) Degradation of sodium dodecyl sulphate in water using solar driven Fenton-like advanced oxidation processes. J Hazard Mater 151:578–584. https://doi.org/10.1016/j.jhazmat.2007.06.025

Behnajady M, Modirshahla N, Hamzavi R (2006) Kinetic study on photocatalytic degradation of C.I. Acid yellow 23 by ZnO photocatalyst. J Hazard Mater 133:226–232. https://doi.org/10.1016/j.jhazmat.2005

Bekkouche S, Mrouani S, Hamdaoui O, Bouhelassa M (2017) Efficient photocatalytic degradation of Safranin O by integrating solar-UV/TiO$_2$/persulfate treatment: implication of sulfate radical in the oxidation process and effect of various water matrix components. J Photochem Photobiol A Chem 345:80–91. https://doi.org/10.1016/j.jphotochem.2017.05.028

Bilal M, Rasheed T, Iqbal HM, Hu H, Wang W, Zhang X (2018) Toxicological assessment and UV/TiO$_2$-based induced degradation profile of reactive black 5 dye. Environ Manag 61(1):171–180. https://doi.org/10.1007/s00267-017-0948-7

Blanco J, Malato S, Fernández P, Vidal A, Morales A, Trincado P, Oliveira JC, Minero C, Musci M, Casalle C, Brunotte M, Tratzky S, Dischinger N, Funken KH, Sattler C, Vincent M, Collares-Pereira M, Mendes JF, Rangel CM (1999) Compound parabolic concentrator technology development to commercial solar detoxification applications. Sol Energy 67:317–330. https://doi.org/10.1016/S0038-092X(00)00078-5

Cerrato G, Bianchi CL, Galli F, Pirola C, Morandi S, Capucci V (2019) Micro-TiO$_2$ coated glass surfaces safely abate drugs in surface water. J Hazard Mater 363:328–334. https://doi.org/10.1016/j.jhazmat.2018.09.057

Daneshvar N, Rasoulifard MH, Khataee AR, Hosseinzadeh F (2007) Removal of C.I. acid orange 7 from aqueous solution by UV irradiation in the presence of ZnO nanopowder. J Hazard Mater 143:95–101. https://doi.org/10.1016/j.jhazmat.2006.08.072

Du GH, Liu ZL, Xia X, Chu Q, Zhang SM (2006) Characterization and application of Fe$_3$O$_4$/SiO$_2$ nanocomposites. J Sol–Gel Sci Technol 39:285–291. https://doi.org/10.1007/s10971-006-7780-5

Dükkancı M (2018) Sono-photo-Fenton oxidation of bisphenol-A over a LaFeO$_3$ perovskite catalyst. Ultrason Sonochem 40:110–116. https://doi.org/10.1016/j.ultsonch.2017.04.040

Epold I, Dulova N (2015) Oxidative degradation of levofloxacin in aqueous solution by S$_2$O$_8$$^{2-}$/Fe^{2+}, S$_2O_8$$^{2-}$/H$_2O_2$ and S$_2$O$_8$$^{2-}$/OH$^-$ processes: a comparative study. J Environ Chem Eng 3:1207–1214. https://doi.org/10.1016/j.jece.2015.04.019

Eskandarian MR, Fazli M, Rasoulifard MH, Choi H (2016) Decomposition of organic chemicals by zeolite-TiO$_2$ nanocomposite supported onto low density polyethylene film under UV-LED powered by solar radiation. Appl Catal B Environ 183:407–416. https://doi.org/10.1016/j.apcatb.2015.11.004

Faisal M, Abu Tariq M, Muneer M (2007) Photocatalysed degradation of two selected dyes in UV-irradiated aqueous suspensions of titania. Dyes Pigments 72:233–239. https://doi.org/10.1016/j.dyepig.2005.08.020

Ghalamchi L, Rasoulifard MH, Seyed Dorraji MS, Pourata R (2017) Solar photocatalytic oxidation of an azo dye with immobilized TiO$_2$/S$_2$O$_8$$^{2-}$ in a component parabolic collector–reactor. Desalin Water Treat 81:223–232. https://doi.org/10.5004/dwt.2017.21005

Ghaly MY, Härtel G, Mayer R, Haseneder R (2001) Photochemical oxidation of p-chlorophenol by UV/H$_2$O$_2$ and photo-Fenton process. A comparative study. Waste Manag 21:41–47. https://doi.org/10.1016/S0956-053X(00)00070-2

Hassan M, Zhao Y, Xie B (2016) Employing TiO$_2$ photocatalysis to deal with landfill leachate: current status and development. Chem Eng J 285:264–275. https://doi.org/10.1016/j.cej.2015.09.093

Khaki MRD, Shafeeyan MS, Raman AAA, Daud WMAW (2018) Evaluating the efficiency of nano-sized Cu doped TiO$_2$/ZnO photocatalyst under visible light irradiation. J Mol Liq 258:354–365. https://doi.org/10.1016/j.molliq.2017.11.030

Khataee AR, Fathinia M, Aber S, Zarei M (2010) Optimization of photocatalytic treatment of dye solution on supported TiO2 nanoparticles by central composite design: intermediates identification. J Hazard Mater 181:886–897. https://doi.org/10.1016/j.jhazmat.2010.05.096

Lv Y, Ding Y, Zhou J et al (2009a) Preparation, characterization, and photocatalytic activity of N, S-codoped TiO$_2$

nanoparticles. J Am Ceram Soc 92:938–941. https://doi.org/10.1111/j.1551-2916.2009.02951.x

Lv Y, Yu L, Huang H et al (2009b) Preparation, characterization of P-doped TiO_2 nanoparticles and their excellent photocatalystic properties under the solar light irradiation. J Alloys Compds 488:314–319. https://doi.org/10.1016/j.jallcom.2009.08.116

Marandi R, Olya ME, Vahid B, Khosravi M, Hatami M (2012) Kinetic modeling of photocatalytic degradation of an azo dye using nano-TiO_2/polyester. Environ Eng Sci 29:957–963. https://doi.org/10.1089/ees.2011.0266

Modirshahla N, Behnajady MA, Ghanbary F (2007) Decolorization and mineralization of CI acid yellow 23 by Fenton and photo-Fenton processes. Dyes Pigments 73:305–310. https://doi.org/10.1016/j.dyepig.2006.01.002

Moncayo-Lasso A, Pulgarin C, Benítez N (2008) Degradation of DBPs' precursors in river water before and after slow sand filtration by photo-Fenton process at pH 5 in a solar CPC reactor. Water Res 42:4125–4132. https://doi.org/10.1016/j.watres.2008.07.014

Muruganandham M, Shobana N, Swaminathan M (2006) Optimization of solar photocatalytic degradation conditions of reactive yellow 14 azo dye in aqueous TiO_2. J Mol Catal A Chem 246:154–161. https://doi.org/10.1016/j.molcata.2005.09.052

Nakata K, Fujishima A (2012) TiO_2 photocatalysis: design and applications. J Photochem Photobiol C Photochem Rev 13:169–189. https://doi.org/10.1016/j.jphotochemrev.2012.06.001

Pirhashemi M, Habibi-Yangjeh A (2013) Simple and large scale one-pot method for preparation of AgBr–ZnO nanocomposites as highly efficient visible light photocatalyst. Appl Sur Sci 283:1080–1088. https://doi.org/10.1016/j.apsusc.2013.07.079

Prato-Garcia D, Vasquez-Medrano R, Hernandez-Esparza M (2009) Solar photoassisted advanced oxidation of synthetic phenolic wastewaters using ferrioxalate complexes. Sol Energy 83:306–315. https://doi.org/10.1016/j.solener.2008.08.005

Rasouli F, Aber S, Salari D, Khataee AR (2014) Optimized removal of reactive navy blue SP-BR by organo-montmorillonite based adsorbents through central composite design. Appl Clay Sci 87:228–234. https://doi.org/10.1016/j.clay.2013.11.010

Saien J, Shafiei H, Amisama A (2017) Photo-activated periodate in homogeneous degradation and mineralization of quinoline: optimization, kinetic, and energy consumption. Environ Prog Sustain Energy 36:1621–1627. https://doi.org/10.1002/ep.12615

Sciacca F, Rengifo-Herrera JA, Wéthé J, Pulgarin C (2011) Solar disinfection of wild *Salmonella* sp. in natural water with a 18L CPC photoreactor: detrimental effect of non-sterile storage of treated water. Sol Energy 85:1399–1408. https://doi.org/10.1016/j.solener.2011.03.022

Shahadat M, Teng TT, Rafatullah M, Arshad M (2015) Titanium-based nanocomposite materials: a review of recent advances and perspectives. Colloids Surf B 126:121–137. https://doi.org/10.1016/j.colsurfb.2014.11.049

Sheydaei M, Aber S, Khataee A (2014) Degradation of amoxicillin in aqueous solution using nanolepidocrocite chips/H_2O_2/UV: optimization and kinetics studies. J Ind Eng Chem 20:1772–1778. https://doi.org/10.1016/j.jiec.2013.08.031

Wolfrum EJ, Huang J, Blake DM et al (2002) Photocatalytic oxidation of bacteria, bacterial and fungal spores, and model biofilm components to carbon dioxide on titanium dioxide-coated surfaces. Environ Sci Technol 36:3412–3419. https://doi.org/10.1021/es011423j

Wu S, Sun A, Zhai F, Wang J, Xu W, Zhang Q, Volinsky AA (2011) Fe_3O_4 magnetic nanoparticles synthesis from tailings by ultrasonic chemical co-precipitation. Mater Lett 65:1882–1884. https://doi.org/10.1016/j.matlet.2011.03.065

Yang M, Thompson DW, Meyer GJ (2000) Dual pathways for TiO_2 sensitization by $Na_2[Fe(bpy)(CN)_4]$. Inorg Chem 39:3738–3739. https://doi.org/10.1021/ic000415l

Yousef A, Barakat NAM, Amna T et al (2012) Influence of CdO-doping on the photoluminescence properties of ZnO nanofibers: effective visible light photocatalyst for waste water treatment. J Lumin 132:1668–1677. https://doi.org/10.1016/j.jlumin.2012.02.031

Zamiri R, Singh B, Bdikin I et al (2014) Influence of Mg doping on dielectric and optical properties of ZnO nano-plates prepared by wet chemical method. Solid State Commun 195:74–79. https://doi.org/10.1016/j.ssc.2014.07.011

Zhan J, Zhang H, Zhu G (2014) Magnetic photocatalysts of cenospheres coated with Fe_3O_4/TiO_2 core/shell nanoparticles decorated with Ag nanopartilces. Ceram Int 40:8547–8559. https://doi.org/10.1016/j.ceramint.2014.01.069